

# FLUORESCENCE MICROSCOPY IMAGE SEGMENTATION USING CONVOLUTIONAL NEURAL NETWORK WITH GENERATIVE ADVERSARIAL NETWORKS

Chichen Fu\*   Soonam Lee\*   David Joon Ho\*   Shuo Han\*  
Paul Salama†   Kenneth W Dunn‡   Edward J. Delp\*

\*Video and Image Processing Laboratory  
School of Electrical and Computer Engineering  
Purdue University  
West Lafayette, Indiana

†Department of Electrical and  
Computer Engineering  
Indiana University-Purdue University  
Indianapolis, Indiana

‡Division of Nephrology  
School of Medicine  
Indiana University  
Indianapolis, Indiana

## ABSTRACT

Recent advance in fluorescence microscopy enables acquisition of 3D image volumes with better quality and deeper penetration into tissue. Segmentation is a required step to characterize and analyze biological structures in the images. 3D segmentation using deep learning has achieved promising results in microscopy images. One issue is that deep learning techniques require a large set of groundtruth data which is impractical to annotate manually for microscopy volumes. This paper describes a 3D nuclei segmentation method using 3D convolutional neural networks. A set of synthetic volumes and the corresponding groundtruth volumes are generated automatically using a generative adversarial network. Segmentation results demonstrate that our proposed method is capable of segmenting nuclei successfully in 3D for various data sets.

**Index Terms**— nuclei segmentation, fluorescence microscopy, 3D convolutional neural network, synthetic data generation, generative adversarial networks

## 1. INTRODUCTION

Fluorescence microscopy is a type of an optical microscopy that uses fluorescence to image 3D subcellular structures [1, 2]. Three dimensional segmentation is needed to quantify and characterize cells, nuclei or other biological structures since manual segmentation is tedious.

Various nuclei segmentation methods have been investigated in the last few decades. Active contours [3, 4] which minimizes an energy functional to fit desired shapes has been one of the most successful methods in microscopy image analysis. Since active contours uses the image gradient to evolve a contour to the boundary of an object, this method can be sensitive to noise and highly dependent on initial contour placement. In [5] an external energy term which convolves a controllable vector field kernel with an image edge map was introduced to address these problems. In [6] 2D region-based active contours using image intensity to identify a region of interest was described. This achieves better performance on noisy image and is relatively independent of the initial curve placement. Extending this to 3D, [7] described 3D segmentation of a rat kidney structure. This technique was further extended to address the problem of 3D intensity inhomogeneity [8]. However, these energy functional based methods cannot distinguish various structures [9]. Alternatively, [10, 11] described a method known as Squash to solve the en-

ergy minimization problem from a generalized linear model to couple image restoration and segmentation. In addition, [12] described multidimensional segmentation using random seeds combined with multi-resolution, multi-scale, and region-growing technique.

Convolutional neural network (CNN) has been recently used to address problems in segmentation and object identification [13]. Various approaches, based on CNNs, have been used in the biomedical area [14]. U-Net [15] is a 2D CNN which uses an encoder-decoder architecture to segment cells in light microscopy images. In [16] a multi-input multi-output CNN for cell segmentation in fluorescence microscopy images to segment various size and intensity cells was described. Since these approaches [15, 16] are 2D segmentation methods, they may fail to produce reasonable segmentation in 3D. More specifically, stacking these 2D segmentation images into 3D volume may result in misalignment in the depth direction [7]. A combination of a 2D CNN nuclei segmentation and 3D refinement processing was used for 3D segmentation in [17]. Similarly, [18] trained three networks from different directions in a volume and combined these three results to produce a form of 3D segmentation. A 3D U-Net [19] was introduced to identify 3D structures by extending the architecture of [15] to 3D. However, this approach requires manually annotated groundtruth to train the network. Generating groundtruth for 3D volumes is tedious and is generally just done on 2D slices, obtaining true 3D groundtruth volumes are impractical. One way to address this is to use synthetic ground truth data [20, 21]. We introduced a method that segments nuclei by training a 3D CNN with synthetic microscopy volumes in [22].

Generating realistic synthetic microscopy data remains a challenging problem since various types of noises and biological structures with different shapes are present and need to be modeled. Recently, [23] proposed a generative adversarial network (GAN) to address image-to-image translation problems using two adversarial networks, a generative network and a discriminative network. In particular, the discriminative network learns a loss function to distinguish whether the output image is real or fake whereas the generative network tries to minimize this loss function. One of the extensions of GANs is Pix2Pix [24] which uses conditional GANs to learn the relationship between the input image and output image that can generate realistic images. One issue with Pix2Pix [24] is that it still requires paired training data to train the networks. In [25] coupled GANs (CoGAN) for learning the joint distribution of multi-domain images without having the corresponding groundtruth images was introduced. Later, a cycle-consistent adversarial networks (CycleGAN) [26] employed a cycle consistent term in the adversarial loss function for image generation without using paired training data.

In this paper, we present a 3D segmentation method to identify and segment nuclei in fluorescence microscopy volumes without the

This work was partially supported by a George M. O'Brien Award from the National Institutes of Health under grant NIH/NIDDK P30 DK079312 and the endowment of the Charles William Harrison Distinguished Professorship at Purdue University.

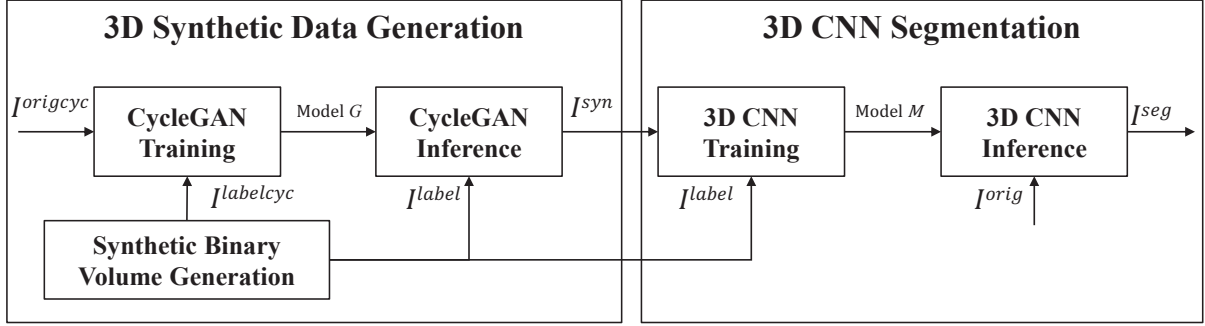


Fig. 1. Block diagram of the proposed approach for 3D nuclei segmentation

need of manual segmented groundtruth volumes. Three dimensional synthetic training data is generated using CycleGAN [26]. A 3D CNN network is then trained using 3D synthetic data to segment nuclei structures. Our method is evaluated using hand segmented groundtruth volumes of real fluorescence microscopy data from a rat kidney. Our data are collected using two-photon microscopy with nuclei labeled with Hoechst 33342 stain.

## 2. PROPOSED METHOD

Figure 1 shows a block diagram of our method. We denote  $I$  as a 3D image volume of size  $X \times Y \times Z$ . Note that  $I_{z_p}$  is a  $p^{\text{th}}$  focal plane image, of size  $X \times Y$ , along the  $z$ -direction in a volume, where  $p \in \{1, \dots, Z\}$ . Note also that  $I^{\text{orig}}$  and  $I^{\text{seg}}$  be the original fluorescence microscopy volume and segmented volume, respectively. In addition, let  $I_{(q_i:q_f, r_i:r_f, p_i:p_f)}$  be a subvolume of  $I$ , whose  $x$ -coordinate is  $q_i \leq x \leq q_f$ ,  $y$ -coordinate is  $r_i \leq y \leq r_f$ ,  $z$ -coordinate is  $p_i \leq z \leq p_f$ , where  $q_i, q_f \in \{1, \dots, X\}$ ,  $r_i, r_f \in \{1, \dots, Y\}$ ,  $p_i, p_f \in \{1, \dots, Z\}$ ,  $q_i \leq q_f$ ,  $r_i \leq r_f$ , and  $p_i \leq p_f$ . For example,  $I_{(241:272, 241:272, 131:162)}^{\text{seg}}$  is a subvolume of a segmented volume,  $I^{\text{seg}}$ , where the subvolume is cropped between 241<sup>st</sup> slice and 272<sup>nd</sup> slice in  $x$ -direction, between 241<sup>st</sup> slice and 272<sup>nd</sup> slice in  $y$ -direction, and between 131<sup>st</sup> slice and 162<sup>nd</sup> slice in  $z$ -direction.

As shown in Figure 1, our proposed method consists of two steps: 3D synthetic data generation and 3D CNN segmentation. We first generate synthetic binary volumes,  $I^{\text{labelcyc}}$ , and then use them with a subvolume of the original image volumes,  $I^{\text{origcyc}}$ , to train a CycleGAN network and obtain a generative model denoted as model  $G$ . This model  $G$  is used with another set of synthetic binary volume,  $I^{\text{label}}$ , to generate corresponding synthetic 3D volumes,  $I^{\text{syn}}$ . For 3D CNN segmentation, we can utilize these paired  $I^{\text{syn}}$  and  $I^{\text{label}}$  to train a 3D CNN and obtain model  $M$ . Finally, the 3D CNN model  $M$  is used to segment nuclei in  $I^{\text{orig}}$  to produce  $I^{\text{seg}}$ .

### 2.1. 3D Synthetic Data Generation

Three dimensional synthetic data generation consists of synthetic binary volume generation, CycleGAN training, and CycleGAN inferences. In synthetic binary volume generation, nuclei are assumed to have an ellipsoidal shape, multiple nuclei are randomly generated in different orientations and locations in a volume [22]. In CycleGAN training, the CycleGAN is trained to generate a synthetic microscopy volume. CycleGAN uses a combination of discriminative networks and generative networks to solve a minimax problem by adding cycle consistency loss to the original GAN loss function as [23, 26]:

$$\begin{aligned} \mathcal{L}(G, F, D_1, D_2) = & \mathcal{L}_{\text{GAN}}(G, D_1, I^{\text{labelcyc}}, I^{\text{origcyc}}) \\ & + \mathcal{L}_{\text{GAN}}(F, D_2, I^{\text{origcyc}}, I^{\text{labelcyc}}) + \lambda \mathcal{L}_{\text{cyc}}(G, F) \end{aligned}$$

where

$$\begin{aligned} \mathcal{L}_{\text{GAN}}(G, D_1, I^{\text{labelcyc}}, I^{\text{origcyc}}) = & \mathbb{E}_{I^{\text{origcyc}}} [\log(D_1(I^{\text{origcyc}}))] \\ & + \mathbb{E}_{I^{\text{labelcyc}}} [\log(1 - D_1(G(I^{\text{labelcyc}})))] \end{aligned}$$

$$\begin{aligned} \mathcal{L}_{\text{GAN}}(F, D_2, I^{\text{origcyc}}, I^{\text{labelcyc}}) = & \mathbb{E}_{I^{\text{labelcyc}}} [\log(D_2(I^{\text{labelcyc}}))] \\ & + \mathbb{E}_{I^{\text{origcyc}}} [\log(1 - D_2(F(I^{\text{origcyc}})))] \end{aligned}$$

$$\begin{aligned} \mathcal{L}_{\text{cyc}}(G, F) = & \mathbb{E}_{I^{\text{labelcyc}}} [\|F(G(I^{\text{labelcyc}})) - I^{\text{labelcyc}}\|_1] \\ & + \mathbb{E}_{I^{\text{origcyc}}} [\|G(F(I^{\text{origcyc}})) - I^{\text{origcyc}}\|_1]. \end{aligned}$$

Here,  $\lambda$  is a weight coefficient and  $\|\cdot\|_1$  is  $L_1$  norm. In our proposed method,  $\lambda$  is set to 10. Note that Model  $G$  maps  $I^{\text{labelcyc}}$  to  $I^{\text{origcyc}}$  while Model  $F$  maps  $I^{\text{origcyc}}$  to  $I^{\text{labelcyc}}$ . Also,  $D_1$  distinguishes between  $I^{\text{origcyc}}$  and  $G(I^{\text{labelcyc}})$  while  $D_2$  distinguishes between  $I^{\text{labelcyc}}$  and  $F(I^{\text{origcyc}})$ .  $G(I^{\text{labelcyc}})$  is an original like microscopy volume generated by model  $G$  and  $F(I^{\text{origcyc}})$  is generated by model  $F$  that looks similar to a synthetic binary volume. Here,  $I^{\text{origcyc}}$  and  $I^{\text{labelcyc}}$  are unpaired set of images. In CycleGAN inference,  $I^{\text{syn}}$  is generated using the model  $G$  on  $I^{\text{label}}$ . As previously indicated  $I^{\text{syn}}$  and  $I^{\text{label}}$  are a paired set of images. Here,  $I^{\text{label}}$  is served as a groundtruth volume corresponding to  $I^{\text{syn}}$ .

### 2.2. 3D CNN Segmentation

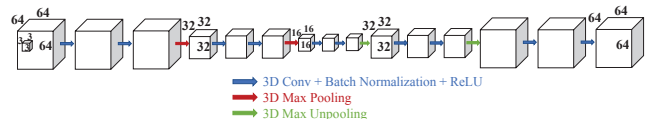


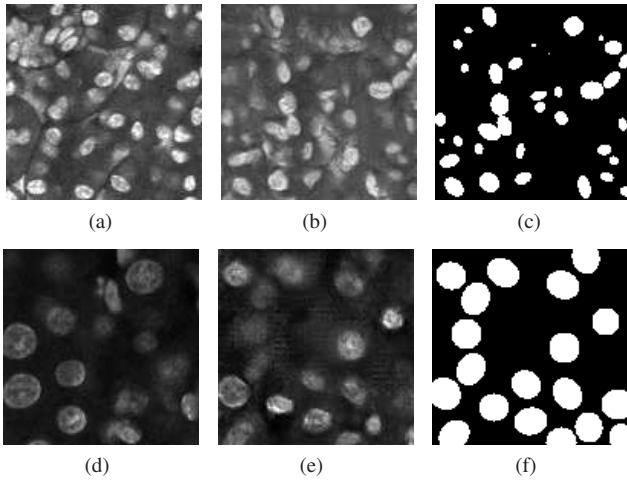
Fig. 2. Architecture of our 3D CNN

Figure 2 shows the architecture of an encoder-decoder convolutional neural network. The filter size of each 3D convolution is  $3 \times 3 \times 3$ . To maintain the same size of volume during 3D convolution, a voxel padding of  $1 \times 1 \times 1$  is used in each convolution. A 3D batch normalization [27] and a rectified-linear unit (ReLU) activation function are employed after each 3D convolution. In the encoder, a 3D max-pooling uses  $2 \times 2 \times 2$  with stride of 2 is used. In the decoder, feature information is retrieved using 3D max unpoolings. Each 3D max unpooling uses the indices saved from each corresponding 3D max pooling. The network takes a grayscale input volume with size of  $64 \times 64 \times 64$  and produces an voxelwise classified 3D volume with the same size of the input volume. Our

architecture is implemented in Torch [28] using stochastic gradient descent (SGD). To train our model  $M$ , 64 pairs of synthetic microscopy volumes,  $I^{syn}$ , and synthetic binary volumes,  $I^{label}$  are used.

For the 3D CNN inference step we first zero-padded  $I^{orig}$  by 16 voxels on the boundaries. A 3D window with size of  $64 \times 64 \times 64$  is used to segment nuclei. Since the zero padded  $I^{orig}$  is bigger than the 3D window, the 3D windows is slided to  $x$ ,  $y$ , and  $z$ -directions by 32 voxels on zero-padded  $I^{orig}$  [22]. Nuclei partially observed on boundaries of the 3D window may not be segmented correctly. Hence, only the central subvolume of the output of the 3D window with size of  $32 \times 32 \times 32$  is used to generate the corresponding subvolume of  $I^{seg}$  with size of  $32 \times 32 \times 32$ . This process is done until the 3D window maps an entire volume.

### 3. EXPERIMENTAL RESULTS



**Fig. 3.** Slices of the original volume and the corresponding synthetic volume for Data-I and Data-II (a) original image of Data-I, (b) synthetic image of Data-I, (c) synthetic binary image of Data-I (d) original image of Data-II, (e) synthetic image of Data-II, (f) synthetic binary image of Data-II.

We tested our proposed method on two different rat kidney data sets. These data sets contain grayscale images of size  $X = 512 \times Y = 512$ . Data-I consists of  $Z = 512$  images, Data-II consist of  $Z = 64$ <sup>1</sup>

We trained the CycleGAN to generate synthetic volumes for Data-I and Data-II, respectively. A  $128 \times 128 \times 128$  synthetic binary volume for Data-I denoted as  $I^{labelcycData-I}$  and a  $128 \times 128 \times 300$  subvolume of original microscopy volume of Data-I denoted as  $I^{origcycData-I}$  were used to train model  $G^{Data-I}$ . Similarly, a  $128 \times 128 \times 128$  synthetic binary volume for Data-II denoted as  $I^{labelcycData-II}$  and a  $128 \times 128 \times 32$  subvolume of original microscopy volume of Data-II denoted as  $I^{origcycData-II}$  were used to train model  $G^{Data-II}$ . We generated 8 sets of  $128 \times 128 \times 128$  synthetic binary volumes,  $I^{labelData-I}$  and  $I^{labelData-II}$  where  $I^{labelData-I}$  and  $I^{labelData-II}$  are generated according to different size of nuclei in Data-I and Data-II, respectively. By using the model  $G^{Data-I}$  on  $I^{labelData-I}$ , 8 pairs of synthetic binary volumes,  $I^{labelData-I}$ , and corresponding synthetic microscopy volumes,  $I^{synData-I}$ , of size of  $128 \times 128 \times 128$  were obtained. Similarly, by

<sup>1</sup>Data-I was provided by Malgorzata Kamocka of the Indiana Center for Biological Microscopy.

using model  $G^{Data-II}$  on  $I^{labelData-II}$ , 8 pairs of  $I^{labelData-II}$  and corresponding  $I^{synData-II}$ , of size of  $128 \times 128 \times 128$  were obtained. Since our 3D CNN architecture takes volumes of size of  $64 \times 64 \times 64$ , we divided  $I^{labelData-I}$ ,  $I^{synData-I}$ ,  $I^{labelData-II}$ , and  $I^{synData-II}$  into adjacent non overlapping  $64 \times 64 \times 64$ . Thus, we have 64 pairs of synthetic binary volumes and corresponding synthetic microscopy volumes per each data to train our 3D CNN network. Note that these 64 synthetic binary volumes per each data are used as groundtruth volumes to be paired with corresponding synthetic microscopy volumes. Model  $M^{Data-I}$  and  $M^{Data-II}$  are then generated.

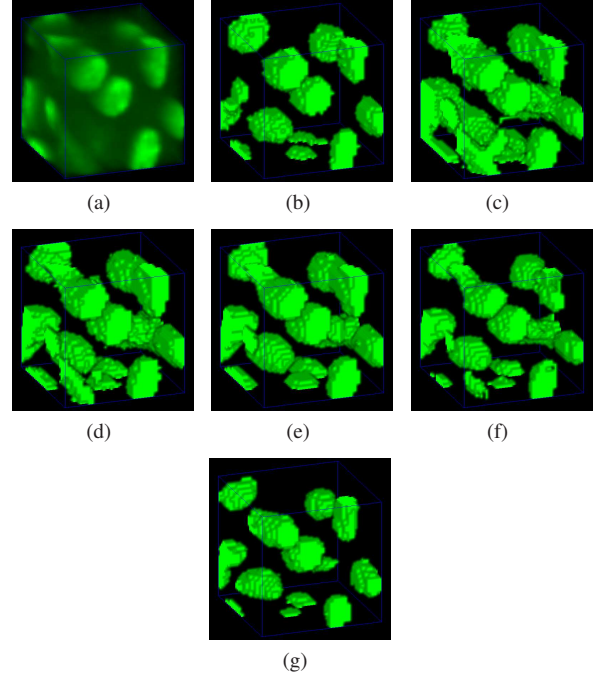


**Fig. 4.** 3D visualization of subvolume 1 of Data-I using VoxX [29] (a) original volume (b) 3D ground truth volume, (c) 3D active surfaces from [7], (d) 3D active surfaces with inhomogeneity correction from [8], (e) 3D Squash from [10, 11], (f) 3D CNN from [22], (g) proposed method

Figure 3 shows the synthetic images generated by the proposed method. The left column indicates original images whereas middle column shows synthetic images generated artificially from corresponding synthetic binary images shown in right column. As can be seen from Figure 3, the synthetic images reflect characteristics of the original microscopy images such as background noise, nuclei shape, orientation and intensity. More importantly, having synthetic binary images, our proposed method is capable of generating corresponding synthetic microscopy images which can be used to train a 3D CNN.

Our method was compared to other 3D segmentation methods including 3D active surface [7], 3D active surface with inhomogeneity correction [8], 3D Squash [10, 11], and our previously described of 3D CNN [22]. Three original 3D subvolumes of Data-I were selected to evaluate the performance of our method. We denote the original volume as subvolume 1 ( $I_{(241:272,241:272,31:62)}^{orig}$ ), subvolume 2 ( $I_{(241:272,241:272,131:162)}^{orig}$ ), and subvolume 3 ( $I_{(241:272,241:272,231:262)}^{orig}$ ), respectively. Corresponding groundtruth of each subvolume was hand segmented. VoxX [29] was used to visualize the segmentation results in 3D and



**Table 1.** Accuracy, Type-I and Type-II errors for known methods and our method on subvolume 1, subvolume 2 and subvolume 3 of Data-I

Method	Subvolume 1			Subvolume 2			Subvolume 3		
	Accuracy	Type-I	Type-II	Accuracy	Type-I	Type-II	Accuracy	Type-I	Type-II
Method [7]	84.09%	15.68%	0.23%	79.25%	20.71%	0.04%	76.44%	23.55%	0.01%
Method [8]	87.36%	12.44%	0.20%	86.78%	13.12%	0.10%	83.47%	16.53%	0.00%
Method [10, 11]	90.14%	9.07%	0.79%	88.26%	11.67%	0.07%	87.29%	12.61%	0.10%
Method [22]	92.20%	5.38%	2.42%	92.32%	6.81%	0.87%	94.26%	5.19%	0.55%
Proposed Method	93.05%	3.09%	3.87%	91.30%	5.64%	3.06%	94.17%	3.96%	1.88%

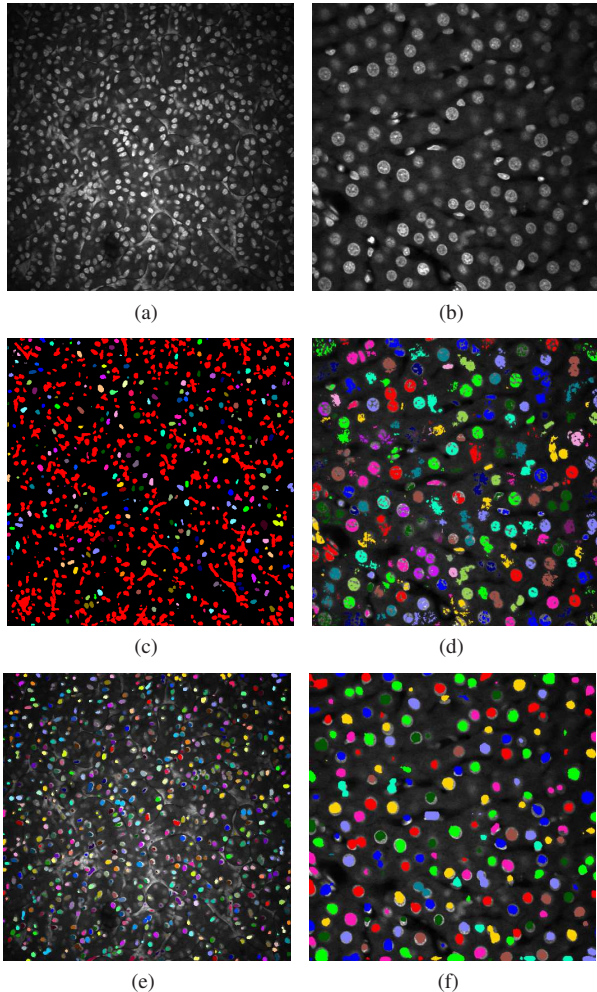


**Fig. 5.** Original images and their color coded segmentation results of Data-I and Data-II (a) Data-I  $I_{z66}^{orig}$ , (b) Data-II  $I_{z31}^{orig}$ , (c) Data-I  $I_{z66}^{seg}$  using [22], (d) Data-II  $I_{z31}^{seg}$  using [22], (e) Data-I  $I_{z66}^{seg}$  using the proposed method, (f) Data-II  $I_{z31}^{seg}$  using proposed method

compared to the manually annotated volumes. In Figure 4, 3D visualizations of the hand segmented subvolume 1 and the corresponding segmentation results for various methods were presented. As seen from the 3D visualization in Figure 4, our proposed method shows the best performance among presented methods visually compared to hand segmented groundtruth volume. Our proposed method captures only nuclei structure whereas other presented methods falsely detect non-nuclei structures as nuclei.

All segmentation results were evaluated quantitatively based on voxel accuracy, Type-I error and Type-II error metrics, using 3D hand segmented volumes. Here, accuracy =  $\frac{n_{TP} + n_{TN}}{n_{total}}$ , Type-I error =  $\frac{n_{FP}}{n_{total}}$ , Type-II error =  $\frac{n_{FN}}{n_{total}}$ , where  $n_{TP}$ ,  $n_{TN}$ ,  $n_{FP}$ ,

$n_{FN}$ ,  $n_{total}$  are defined to be the number of true-positives (voxels segmented as nuclei correctly), true-negatives (voxels segmented as background correctly), false-positives (voxels falsely segmented as nuclei), false-negatives (voxels falsely segmented as background), and the total number of voxels in a volume, respectively.

The quantitatively evaluations for the subvolumes are shown in Table 1. Our proposed method achieves similar accuracy to our previous method described in [22]. However, as observed from Figure 5, the color coded segmentation results of proposed method outperforms method [22] in terms of identifying nuclei regions. The smaller Type-I error shows our proposed method successfully rejects non-nuclei structures during segmentation. Since our proposed method tends to under segments nuclei structures, Type-II errors of our proposed method are higher compared to other methods. To make this clear, segmentation results were color coded using 3D connected component labeling and overlaid on the original volumes. Our previous method [22] cannot distinguish between nuclei and non-nuclei structures including noise. This is especially recognizable from segmentation results of Data-I in which multiple nuclei and non-nuclei structures are colored with the same color. Conversely, since the proposed method uses synthetic data that reflects characteristics of original microscopy volume to train the 3D CNN to segment nuclei structure, the proposed method is capable of rejecting non-nuclei structures shown in Figure 5.

#### 4. CONCLUSION

In this paper we presented a 3D CNN nuclei segmentation method using paired synthetic volumes. The training was done using synthetic volumes generated from a CycleGAN network. We compared our proposed method to various segmentation methods and with manually annotated 3D groundtruth from real data. The experimental results indicate that our method can successfully distinguish between non-nuclei and nuclei structure and capture nuclei regions well from various microscopy volumes. In the future, we plan to improve our method by incorporating shape information to separate overlapping nuclei to individuals.

#### 5. REFERENCES

- [1] C. Vonesch, F. Aguet, J. Vonesch, and M. Unser, “The colored revolution of bioimaging,” *IEEE Signal Processing Magazine*, vol. 23, no. 3, pp. 20–31, May 2006.
- [2] K. W. Dunn, R. M. Sandoval, K. J. Kelly, P. C. Dagher, G. A. Tanner, S. J. Atkinson, R. L. Bacallao, and B. A. Molitoris, “Functional studies of the kidney of living animals using multicolor two-photon microscopy,” *American Journal of Physiology-Cell Physiology*, vol. 283, no. 3, pp. C905–C916, September 2002.
- [3] M. Kass, A. Witkin, and D. Terzopoulos, “Snakes: Active contour models,” *International Journal of Computer Vision*, vol. 1, no. 4, pp. 321–331, January 1988.

- [4] R. Delgado-Gonzalo, V. Uhlmann, D. Schmitter, and M. Unser, "Snakes on a plane: A perfect snap for bioimage analysis," *IEEE Signal Processing Magazine*, vol. 32, no. 1, pp. 41–48, January 2015.
- [5] B. Li and S. T. Acton, "Active contour external force using vector field convolution for image segmentation," *IEEE Transactions on Image Processing*, vol. 16, no. 8, pp. 2096–2106, August 2007.
- [6] T. F. Chan and L. A. Vese, "Active contours without edges," *IEEE Transactions on Image Processing*, vol. 10, no. 2, pp. 266–277, February 2001.
- [7] K.S. Lorenz, P. Salama, K.W. Dunn, and E.J. Delp, "Three dimensional segmentation of fluorescence microscopy images using active surfaces," *Proceedings of the IEEE International Conference on Image Processing*, pp. 1153–1157, September 2013, Melbourne, Australia.
- [8] S. Lee, P. Salama, K. W. Dunn, and E. J. Delp, "Segmentation of fluorescence microscopy images using three dimensional active contours with inhomogeneity correction," *Proceedings of the IEEE International Symposium on Biomedical Imaging*, pp. 709–713, April 2017, Melbourne, Australia.
- [9] S. Lee, P. Salama, K. W. Dunn, and E. J. Delp, "Boundary fitting based segmentation of fluorescence microscopy images," *Proceedings of the IS&T/SPIE Conference on Imaging and Multimedia Analytics in a Web and Mobile World 2015*, pp. 940805–1–10, February 2015, San Francisco, CA.
- [10] G. Paul, J. Cardinale, and I. F. Sbalzarini, "Coupling image restoration and segmentation: A generalized linear model/Bregman perspective," *International Journal of Computer Vision*, vol. 104, no. 1, pp. 69–93, March 2013.
- [11] A. Rizk, G. Paul, P. Incardona, M. Bugarski, M. Mansouri, A. Niemann, U. Ziegler, P. Berger, and I. F. Sbalzarini, "Segmentation and quantification of subcellular structures in fluorescence microscopy images using Squash," *Nature Protocols*, vol. 9, no. 3, pp. 586–596, February 2014.
- [12] G. Srinivasa, M. C. Fickus, Y. Guo, A. D. Linstead, and J. Kovacevic, "Active mask segmentation of fluorescence microscope images," *IEEE Transactions on Image Processing*, vol. 18, no. 8, pp. 1817–1829, August 2009.
- [13] J. Long, E. Shelhamer, and T. Darrell, "Fully convolutional networks for semantic segmentation," *Proceedings of the IEEE Conference on Computer Vision and Pattern Recognition*, pp. 3431–3440, June 2015, Boston, MA.
- [14] G. Litjens, T. Kooi, B. E. Bejnordi, A. A. A. Setio, F. Ciompi, M. Ghafoorian, J. A.W.M. van der Laak, B. van Ginneken, and C. I. Sanchez, "A survey on deep learning in medical image analysis," *arXiv preprint arXiv:1702.05747*, February 2017.
- [15] O. Ronneberger, P. Fischer, and T. Brox, "U-Net: Convolutional networks for biomedical image segmentation," *Proceedings of the Medical Image Computing and Computer-Assisted Intervention*, pp. 231–241, October 2015, Munich, Germany.
- [16] S. E. A. Raza, L. Cheung, D. Epstein, S. Pelengaris, M. Khan, and N. Rajpoot, "MIMO-Net: A multi-input multi-output convolutional neural network for cell segmentation in fluorescence microscopy images," *Proceedings of the IEEE International Symposium on Biomedical Imaging*, pp. 337–340, April 2017, Melbourne, Australia.
- [17] C. Fu, D.J. Ho, S. Han, P. Salama, K.W. Dunn, and E.J. Delp, "Nuclei segmentation of fluorescence microscopy images using convolutional neural networks," *Proceedings of the IEEE International Symposium on Biomedical Imaging*, pp. 704–708, April 2017, Melbourne, Australia.
- [18] A. Prasoon, K. Petersen, C. Igel, F. Lauze, E. Dam, and M. Nielsen, "Deep feature learning for knee cartilage segmentation using a triplanar convolutional neural network," *Proceedings of the Medical Image Computing and Computer-Assisted Intervention*, pp. 246–253, September 2013, Nagoya, Japan.
- [19] O. Cicek, A. Abdulkadir, S.S. Lienkamp, T. Brox, and O. Ronneberger, "3D U-Net: Learning dense volumetric segmentation from sparse annotation," *Proceedings of the Medical Image Computing and Computer-Assisted Intervention*, pp. 424–432, October 2016, Athens, Greece.
- [20] X. Zhang, Y. Fu, A. Zang, L. Sigal, and G. Agam, "Learning classifiers from synthetic data using a multichannel autoencoder," *arXiv preprint arXiv:1503.03163*, pp. 1–11, March 2015.
- [21] I. B. Barbosa, M. Cristani, B. Caputo, A. Rognhaugen, and T. Theoharis, "Looking beyond appearances: Synthetic training data for deep CNNs in re-identification," *arXiv preprint arXiv:1701.03153*, pp. 1–14, January 2017.
- [22] D. J. Ho, C. Fu, P. Salama, K.W. Dunn, and E.J. Delp, "Nuclei segmentation of fluorescence microscopy images using three dimensional convolutional neural networks," *Proceedings of the Computer Vision for Microscopy Image Analysis workshop at Computer Vision and Pattern Recognition*, pp. 834–842, July 2017, Honolulu, HI.
- [23] I. Goodfellow, J. Pouget-Abadie, M. Mirza, B. Xu, D. Warde-Farley, S. Ozair, A. Courville, and Y. Bengio, "Generative adversarial nets," *Proceedings of the Advances in Neural Information Processing Systems*, pp. 2672–2680, December 2014, Montreal, Canada.
- [24] P. Isola, J. Y. Zhu, T. Zhou, and A. A. Efros, "Image-to-image translation with conditional adversarial networks," *Proceedings of the IEEE Conference on Computer Vision and Pattern Recognition*, pp. 5967–5976, July 2017, Honolulu, HI.
- [25] M. Y. Liu and O. Tuzel, "Coupled generative adversarial networks," *Proceedings of the Advances in Neural Information Processing Systems*, pp. 469–477, December 2016, Barcelona, Spain.
- [26] J. Y. Zhu, T. Park, P. Isola, and A. A. Efros, "Unpaired image-to-image translation using cycle-consistent adversarial networks," *arXiv preprint arXiv:1703.10593*, pp. 1–16, March 2017.
- [27] S. Ioffe and C. Szegedy, "Batch normalization: Accelerating deep network training by reducing internal covariate shift," *arXiv preprint arXiv:1502.03167*, March 2015.
- [28] R. Collobert, K. Kavukcuoglu, and C. Farabet, "Torch7: A matlab-like environment for machine learning," *Proceedings of the BigLearn workshop at the Neural Information Processing Systems*, pp. 1–6, December 2011, Granada, Spain.
- [29] J. L. Clendenon, C. L. Phillips, R. M. Sandoval, S. Fang, and K. W. Dunn, "Voxx: A PC-based, near real-time volume rendering system for biological microscopy," *American Journal of Physiology-Cell Physiology*, vol. 282, no. 1, pp. C213–C218, January 2002.